Swansea University
Prifysgol Abertawe

Cronfa
Setting Research Free

Cronfa - Swansea University Open Access Repository

_____

This is an author produced version of a paper published in :
International Journal for Numerical Methods in Engineering

_____

Cronfa URL for this paper:
http://cronfa.swan.ac.uk/Record/cronfa31407

_____

Paper:

_____

The calculation of drag on nano-cylinders

F. Hafezi, R.S. Ransing[*] and R.W. Lewis
Zienkiewicz Centre for Computational Engineering (ZCCE), College of Engineering,
Swansea University, Swansea SA1 8EN, UK

[*]r.s.ransing@swansea.ac.uk

SUMMARY

The study of molecular flows at low Knudsen numbers (~0.1-0.5), over nano-scaled objects of 20-100 nm size is becoming an important area of research. The simulation of fluid-structure interaction at nano-scale is important for understanding the adsorption and drag resistance characteristics of nano devices in the fields of drug delivery, surface cleaning and protein movement.

A novel formulation has been proposed that calculates localised values for both the kinetic and configurational parts of the Irwin-Kirkwood stress tensor at given fixed positions within the computational domain.

Macroscopic properties, such as streaming velocity, pressure and drag coefficients are predicted by modelling the fluid-structure interaction using a moving least-squares method. The gravitation driven molecular flow is examined over three different cross sectional shapes, i.e. diamond, circular and square shaped cylinders; confined within parallel walls, has been simulated for rough and smooth surfaces.

The molecular dynamics formulation has allowed, for the first time, the calculation of localised drag forces over nano-cylinders. The computational simulation has shown that existing methods, including continuum based approaches, significantly underestimate drag coefficients over nano-cylinders. The proposed molecular dynamics formulation has been verified on simulation based tests, as experimental and analytical results are unavailable at this scale.

1. INTRODUCTION

When engineering structures become practical at 50-500nm lengths, the prediction of continuum information such as drag force, drag coefficient, velocity and pressure profiles will become necessary. Molecular biomechanics principles are used to design nano and micro scale devices which generally are, at least, less than 100 nm in one dimension. To put this into context, the red blood cells in human blood have diameters around 6200-8200 nm [1] and a rod shaped *Escherichia coli* bacterium has a length of 2500nm and diameter 800nm [2]. Individual atoms are typically a fraction of a nano-meter whilst a human DNA molecule is 2.2-2.6nm wide [3].

Nano-scale devices, or nano-particles, are made of different materials such as lipids, metals and natural or synthetic polymers. Nano-particles have been employed for therapeutic and diagnostic purposes during the last two decades [4]. Bao et al. [4] suggest that an understanding of mechanical forces at a molecular scale can be used in current medical and technological problems. A study of the mechanical force provides a greater insight into diseases and alternative treatments for medical conditions such as asthma, polycystic kidneys and cancer. For instance, World et al. [5] show that atherosclerotic plaques form in areas which have less wall shear stress. Molecular mechanics can successfully describe the process of protein trafficking via the use of active transport and vesicle movement [6]. The forces 'sensed' by molecules must be understood in order to study molecular movement. The most important forces present at the molecular scale are mechanical, chemical and thermal.

Mechanical (viscous) forces are of fundamental importance in diffusion processes. The drag force sensed by a molecule travelling through a stationary fluid depends on the viscosity of the fluid, the velocity of the molecule and a drag coefficient that is a function of the shape and size of the molecule.

Thermal (collisional) forces are defined as forces that take place when molecules collide with each other, and unlike the mechanical forces that retard molecular movement, thermal forces drive movement [7]. The magnitude of the force due to the collision depends on the momentum of the molecule which is a function of both the mass and velocity of the molecule.

2

Hess and Vogel [8] studied the active transport of molecular shuttles in synthetic environments based on motor proteins. They indicate that the flow fields are able to exert substantial drag forces which are functions of flow velocity and viscosity of the solution.

1.1 POTENTIAL NANO-SCALE APPLICATIONS

A molecular machine can be used as a drug delivery device to transport drugs through the blood stream, lungs and intestines to target specific cancer cells with minimal side effects [9-11]. The efficient targeting of molecules and cells in cancer and inflammation can be achieved by understanding the interactions of nano-materials with the biological environment [12]. Tan et al. [13] studied the motion of spherical and rod-shaped nano-particles from the combined effects of drag forces caused by fluid flow and adhesion forces from ligand-receptor binding. For example, a rod with a point contact with the wall results in a smaller adhesion force and a larger drag force; it can also be washed away easily. It was also observed that nano-particles of rod shape and smaller size have higher binding capabilities due to the larger contact area and smaller drag force.

In spite of the recent progress in nanoscale platforms, nanodevices still have poor targeting capabilities [14, 15]. Guidance techniques have been proposed to increase the targeting capabilities of the nano-particles and to enhance their therapeutic and diagnostic efficacy by integrating sensing and actuation mechanisms on the nano-carrier. In order to improve such mechanisms, many researchers have been developing and investigating applications of magnetic nano-particles [16-18].

Magnetic Resonance Imaging (MRI) guided nano-robotic drug delivery systems are used to localize drug delivery in the human body, at the cellular and sub-cellular level, by producing the required external driving forces to guide the magnetic nano-capsules to a specific target which could perform diagnostic, curative and reconstructive treatments [19-20]. Gupta and Kompella [21] have commented that only particles of size 30-300 nm are able to move through the thinnest sections of the vasculature system and which can target and interact with cells.

An ability to determine drag forces using molecular dynamics simulations can also be used to design pathogen biosensors [22]. Gijs [23] studied the behaviour of magnetic nano-particles

at the molecular scale and their applications in magnetic separation, immune-assays, magnetic resonance imaging, drug delivery and hyperthermia.

The cleaning of structured nano-surfaces is a challenging task that has many applications in industry such as in semiconductor, pharmaceutical and xerographic [24]. The drag force has been used to remove particles in order to clean the structured surface [25]. Nano-scale particles also have a much larger surface area than similar masses of large scale materials. As a result, surface forces such as adhesion, friction, meniscus forces, viscous drag forces and surface tension that are proportional to area, become a thousand times greater than the forces which are proportional to the volume, such as inertial and electromagnetic forces. In addition to the consequence of a large surface-to-volume ratio, these devices are designed for small tolerances, which make them particularly vulnerable to adhesion between adjacent components. Even a slight particulate or chemical contamination present at the interface can become detrimental [26].

The research algorithms presented in this paper are generic. However, the gas used for modelling purpose is a methane gas at 300K and 40MPa [27-28]. Understanding the interaction of methane molecules with graphite, and in particular, with reference to its adsorption and storage in nano- channels and groove sites of two carbon nano-tubes [29] is a relevant application. Such high pressures (e.g. 40 MPa) normally exist at deep ocean beds but have also been reported for methane adsorption and storage in carbon nano-tubes [30]. The aim and objective of the research is explained in the next sub-section followed by the proposed formulation for calculating drag coefficients at nano-scale. The results are described in Section 3 and the paper is concluded in Section 4.

1.2 THE AIM AND OBJECTIVE OF THE RESEARCH

The aim of this research is to predict the drag on nano-devices and/or nano-cylinders placed in gravity driven molecular flows. The objective is to calculate nanoscale fluid pressure values at given positions within the molecular domain. The fluid-structure interaction is simulated by using the first principles of molecular dynamics.

Experimental results on drag coefficients on objects of less than 100nm are not reported in the literature. In the absence of experimental results, it was decided to gain an insight into the

molecular interaction with the wall (e.g. with reference to the roughness of the wall, the external force applied to the fluid and geometry of the wall) with the minimum number of external assumptions that can influence the results. A molecular dynamics model conserves the kinetic energy of individual molecules (NVT assumptions) and hence it was decided to use this method. It was also decided to include the wall, and all geometric variations, within one periodic cell, thus not requiring the Lees-Edwards [31] adjustment at boundaries to superimpose any velocity gradient. The nano-cylinders, confined between two parallel walls, are placed inside a periodic cell. The cell was chosen sufficiently long to justify the use of gravitation driven flow and the application of periodic boundary conditions in the flow direction.

2. DRAG AT NANO-SCALE

The drag force F_d, exerted by the molecular flow on a wall surface, is calculated by integrating the component of stress (pressure) tensor σ parallel to the direction of the flow along the surface.

$$\vec{F} = \iint_s f_s \, ds = \iint_s \sigma \cdot \hat{n} \, ds \tag{1}$$

$$f_s = \begin{bmatrix} f_x \\ f_y \end{bmatrix}_s = \begin{bmatrix} \sigma_{xx} & \tau_{xy} \\ \tau_{yx} & \sigma_{yy} \end{bmatrix} \begin{bmatrix} n_x \\ n_y \end{bmatrix} = \begin{bmatrix} \sigma_{xx} n_x + \tau_{xy} n_y \\ \tau_{yx} n_x + \sigma_{yy} n_y \end{bmatrix} \tag{2}$$

Where σ is the stress tensor and n is the normal to the surface ds.

The drag coefficient, C_d, relates the drag force with the average macroscopic kinetic energy of the flow, i.e.,

$$C_d = \frac{2F_d}{\rho A V^2} \tag{3}$$

Where, F_d is the drag force, ρ is the density of the fluid, A is the cross sectional area of the object in the flow regime and V is the average macroscopic velocity of the fluid.

The pressure is a state variable of the gas and the change in pressure during any process is governed by the laws of thermodynamics. At molecular scales, for an NVT system, the

5

pressure value resulting from a molecule's kinetic energy is given by nK_bT, where n is the number density, K_b is the Boltzmann constant and T is the overall absolute temperature value. At small scales, the contribution from intermolecular forces also needs to be considered. The widely used Irwin-Kirkwood equations (7) and (8) for calculating pressure values at molecular scales quantify contributions as 'kinetic' and 'configurational'. The kinetic contribution is due to the molecular motion whereas, the intermolecular forces generate configurational contributions [19, 24-30].

For a homogeneous fluid, the pressure is hydrostatic and is a scalar quantity. However, the interaction of molecular flow with the wall makes the fluid inhomogeneous and the pressure becomes a second rank tensor as it depends on both the orientation of the wall surface and the direction relative to the wall surface. This is represented as a stress tensor $\sigma_{\alpha\beta}$ with the scalar pressure value given by its trace $P = \dfrac{1}{3}tr\sigma_{\alpha\beta}$. \hfill (4)

The subscript β denotes the stress direction on a surface pointing in the α direction. In a Cartesian co-ordinate system $\sigma_{\alpha\beta}$ is represented as

$$\sigma_{\alpha\beta} = \begin{bmatrix} \sigma_{xx} & \sigma_{xy} & \sigma_{xz} \\ \sigma_{yx} & \sigma_{yy} & \sigma_{yz} \\ \sigma_{zx} & \sigma_{zy} & \sigma_{zz} \end{bmatrix} \hfill (5)$$

The stress tensor $\sigma_{\alpha\beta}$ is decomposed into the kinetic $\sigma_{\alpha\beta}^K$ and configurational $\sigma_{\alpha\beta}^U$ part as follows:

$$\sigma_{\alpha\beta} = \sigma_{\alpha\beta}^K + \sigma_{\alpha\beta}^U \hfill (6)$$

The expression of macroscopic stress tensor, $\sigma_{\alpha\beta}$, in a fluid is derived from the microscopic law of momentum conservation at some point r in the fluid at time t.

The commonly used formulation for $\sigma_{\alpha\beta}^K$ and $\sigma_{\alpha\beta}^U$ is given by the Irving-Kirkwood method [39]. The $\sigma_{\alpha\beta}^K$ and $\sigma_{\alpha\beta}^U$ terms are defined as follows:

$$\sigma_{\alpha\beta} = -\frac{1}{V}\left[m\sum_i (\vec{v}_{i\alpha} - \vec{v}_\alpha)(\vec{v}_{i\beta} - \vec{v}_\beta) + \frac{1}{2}\sum_i\sum_{i \neq j} \vec{r}_{ij\alpha} \vec{F}_{ij\beta} \right] \tag{7}$$

$$\sigma_{\alpha\beta}{}^K = -\frac{1}{V} m\sum_i (\vec{v}_{i\alpha} - \vec{v}_\alpha)(\vec{v}_{i\beta} - \vec{v}_\beta), \quad \sigma_{\alpha\beta}{}^U = -\frac{1}{2V}\sum_i\sum_{i \neq j} \vec{r}_{ij\alpha} \vec{F}_{ij\beta} \tag{8}$$

Where,

m_i: is the mass of particle i

V: volume

$\alpha \ and \ \beta$ are the axes of the Cartesian coordinate system.

$\vec{v}_{i\alpha} \ and \ \vec{v}_{i\beta}$ are the velocity components of particle i in the $\alpha \ and \ \beta$ directions.

$\vec{v}_\alpha \ and \ \vec{v}_\beta$ are streaming velocities for molecules i and j.

$r_{ij\alpha}$: α component of the position vector between particle i and j

$F_{ij\beta}$: β component of the force exerted on particle i by particle j

Note that $\vec{F}_{ij} = \dfrac{\partial u_{ij}}{\partial r_i} = -\dfrac{\partial u_{ij}}{\partial r_j}$ where r_i and r_j are the position vectors of molecules i and j

where as u_{ij} is the intermolecular potential between molecules i and j. Depending on the sign convention used the term $\sigma_{\alpha\beta}^U$ is either assigned as a positive or negative sign [40, 41]. There is no unique method to calculate $\sigma_{\alpha\beta}^K$ and $\sigma_{\alpha\beta}^U$ [25, 32-38, 42, 43]. Some of the recent advancements have been summarised in the row(1) [54], row (2) & row (3) [42] and row (4) [43] of Table 1. The major differences in the formulations are in the calculation of streaming velocity, choice of the cut off region of molecules around a given point of interest and the molecules that are chosen for a contribution to the intermolecular force term.

-------- Include Table 1 here.

2.1 CALCULATION OF THE CONFIGURATIONAL PART OF THE STRESS TENSOR

As shown in the second row of Table 1, Lion and Allen [42] proposed a l_{ij} term, in the configurational part of the stress tensor $\sigma_{\alpha\beta}^U$. The contribution of the intermolecular force to the configuration part was proportional to the part of the line segment contained in the cut off

square. In this work an approximate, but computationally efficient technique, has been proposed. As shown in Figure 1b, l_{ij} is equal to one, 0.5 or zero depending upon whether the segment joining the two molecules is fully, partially or not contained within the cut off square corresponding to the fixed reference position. The proposed approximation is computationally simple. However, it is likely to introduce an error in the final computation where l_{ij} is equal to 0.5 or zero. It is anticipated that the overall error will not be significant as some of the positive and negative contributions may cancel each other. However, it may be argued that future work needs to be undertaken with a detailed comparative analysis to justify this assumption.
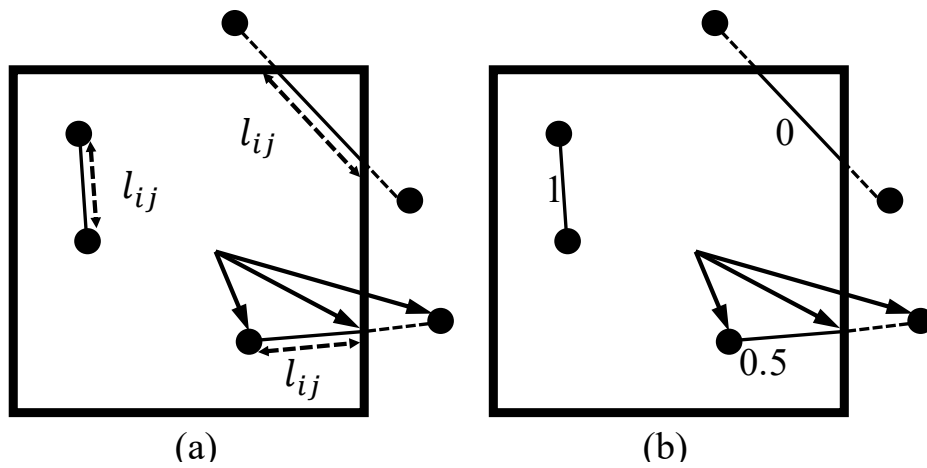

$$(a) \qquad (b)$$

Figure 1. (a) Molecules contribute to the configuration part of the stress tensor $\sigma_{\alpha\beta}^{U}$ depending upon the proportion of the segment l_{ij} contained in the cut off square [42] (b) proposed approximation to l_{ij} values.

2.2 CALCULATION OF SPACIALLY LOCALISED STREAMING VELOCITIES

The mathematical formulation for modelling pair wise interaction among 'fluid-fluid' and 'fluid-wall' molecules is derived using a simple and most commonly used form of the pair wise Lennard-Jones potential, U_{ij} as described by:

$$U_{ij} = 4\varepsilon \left[\left(\frac{\sigma}{r_{ij}} \right)^{12} - \left(\frac{\sigma}{r_{ij}} \right)^{6} \right] \qquad r_{ij} < r_C \qquad (9)$$

Where subscripts i, j correspond to molecules i and j, and r_{ij} is the distance between two molecules. Methane is modelled as a fluid and the solid wall is assumed to be made of carbon molecules. σ represents the collision radius (σ_f for methane is 0.381 nm and σ_w for carbon is 0.34 nm). The subscripts w and f are used to categorise properties for the wall and fluid molecules. The standard Lorenz-Barthelot mixing rule is used to calculate σ_{fw} as 0.3605 nm. ε is the well depth (strength of interaction), and is commonly referred to in the form ε / k_b (k_b is the Boltzmann constant). The corresponding values for methane, carbon and methane-carbon wall, ε_f / k_b, ε_w / k_b and ε_{fw} / k_b are 148.1 K, 28 K and 64.39 K. r_c is the cut off radius and is taken as 2.75 σ. The lattice constant, with value of 3.808A, is used to construct a molecular wall with a Face Centred Cubic (FCC) structure. The potential energy of covalent bonds and interatomic forces in the wall has been ignored. It is assumed that molecular interactions are pairwise additive and molecules are nonreactive and structureless. The wall molecules are assumed to be at a constant temperature and fluid molecules are not allowed to penetrate the wall. The flow is generated by applying predefined molecular acceleration values of (0, 6×10^{11}, 10×10^{11}, 50×10^{11}, 100×10^{11} (m/s^2)) in the flow direction. A Gaussian thermostat is used to control the overall temperature. The molecular dynamic simulation has been performed in three dimensions.

Fixed reference nodes, as shown in Figure 2, are chosen within the molecular dynamics computational domain to derive the macroscopic properties such as streaming velocity or pressure. These nodes are referred to as Moving Least Square (MLS) nodes as the average values for the properties are calculated by extending the one-dimensional MLS method [27,

43]. The methodology is extended to two dimensions as shown in (b)

Figure 2. The proposed circular cut off can be easily extended to a spherical cut off if the variation in the z direction i.e. along the breadth of the channel (the width of the channel is the distance between the parallel walls) becomes important.
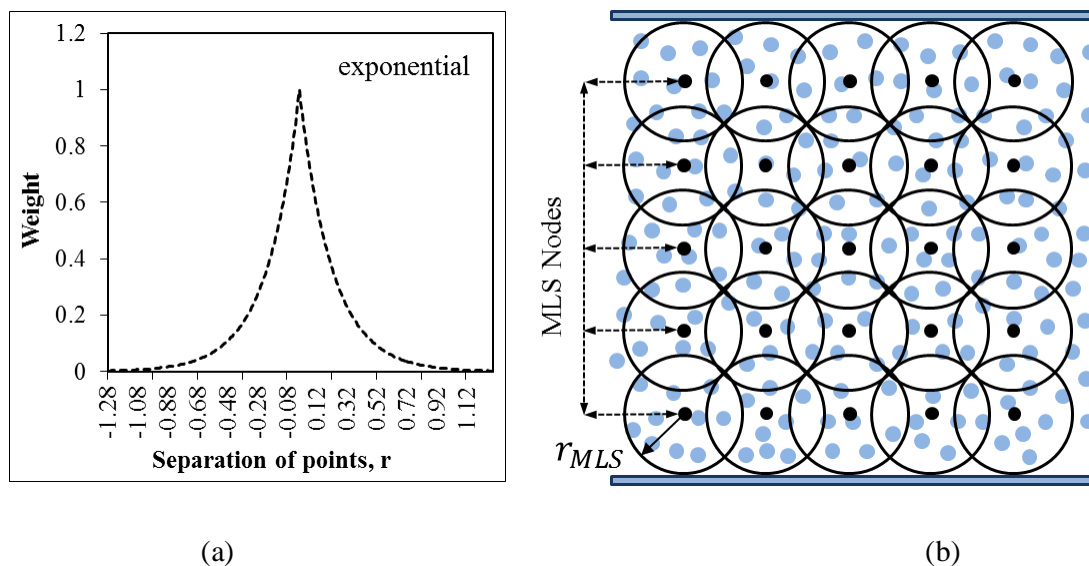

(a)

(b)

Figure 2 (a). Weighting function with a unit value at the MLS node and zero after the cut off radius. (b) A two dimensional array of MLS nodes with cut off circles shown over the schematic molecules in the background.

Equation 10 is used to calculate the pressure values at each MLS node at a given time step. The cut off circle, shown around each MLS node, determines the number of molecules chosen for calculating the macroscopic properties, such as velocity and pressure, at the corresponding MLS nodes. This strategy compares well with the Gaussian kernel (Φ) used to spatially smoothen the microscopic data [44].

The time step for the molecular dynamics simulation is taken as 2 fs. Dyson et.al. [27] have shown that this time step value is an optimal value for a very similar problem. The molecular data (molecular positions and velocity vectors) is collected at every 0.0003 ns and used to calculate the average MLS nodal values using a weighting function as described in (b)

Figure 2. MLS nodal values (macroscopic velocity vectors and stress tensors) are updated at every 0.05ns. The nodal values are averaged for a 0.2 ns period. The sample results are shown in Figure 9 as dotted plots. In other words, each dotted curve, shown in Figure 9, represents a cumulative average in the 0.2 ns period. Over two million time steps of 2fs were used for a simulation run of 2.8ns to reach a steady flow (equilibrium) condition. The steady state response, shown as the continuous curve in Figure 9, is the average of these cumulative averages taken over the production phase of 2.8 ns. The average MLS nodal values are used in Equation 10 and the average of all the MLS nodal values is used to calculate the average overall macroscopic velocity value (Equation 6).
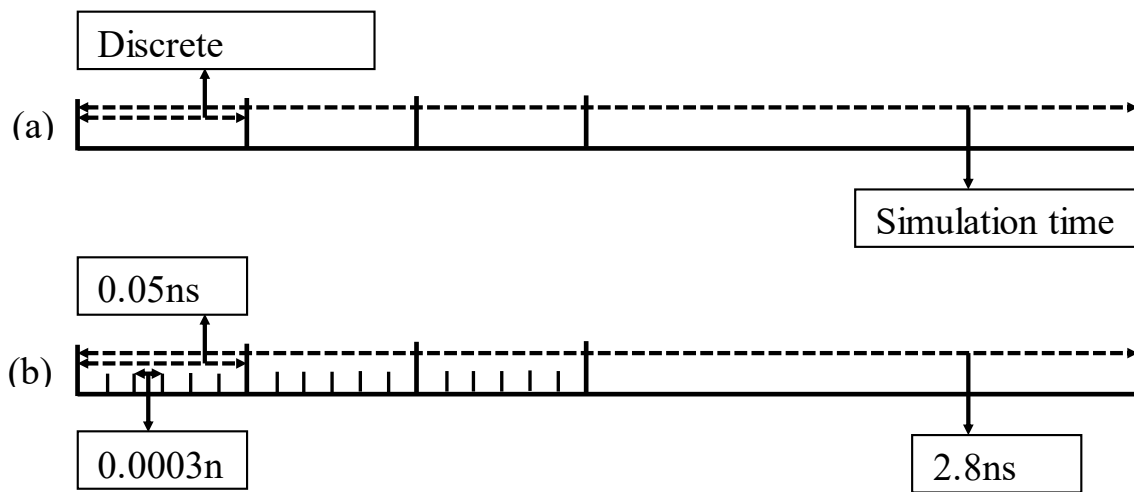

Figure 3. The MLS nodal values are calculated at every 0.05 ns using molecular data captured at every 0.0003 ns. The time step used in the molecular dynamics simulation is 2 fs. The equilibrium properties are averaged in the production stage between 1.12ns and 2.8 ns.

2.3 MODELLING THE FLUID-WALL INTERACTION

Lauga, Brenner and Stone [45] argue that the continuum concept of a no-slip boundary condition at the solid-liquid interface cannot be derived from sound first principles at nano-scales. The slip behaviour at the solid liquid interface at this scale is complex and depends on a number of factors such as wetting conditions, shear rate, pressure, surface energy, surface roughness, dissolved gas, molecular shape and size, probe size and viscosity. The effect of slip and wall surface roughness, on the macroscopic velocity distribution of molecular flow in nano/micro channels, are areas of active research [28, 43, 46-49]. The authors are not aware

of the availability of experimental data to characterize the slip behavior at a 100nm length scale.

The idealisation of molecular walls to capture surface roughness, or molecular corrugation, by introducing different types of molecular obstructions to the wall has been used in the literature [50-52]. The molecular walls, or nanotubes, were constructed with a defined molecular or lattice structure. However, the assumption in this research is that when wall dimensions are reduced from a continuum to sub-micron or nano-scales, the molecular walls no longer follow a defined molecular structure. This hypothesis is proposed after studying the images of atomically smooth, freshly cleaved mica surfaces taken by an Atomic Force Microscopy (AFM) technique [53]. Hence, in this research it is hypothesized that such structured molecular obstructions do not accurately represent the wall roughness at nano-scale.

Sokhan et al. [28] proposed a solid wall with a slip condition at the boundary to simulate the steady state Poiseuille flow. The nano-scale wall is assumed as a continuum wall. When molecules collide with the continuum wall, a fraction of the molecules, categorized by Maxwell's coefficient f, are thermalized [54]. They estimated the value f by analysing the velocity profiles obtained from an equivalent simulation with a molecular wall with two graphene layers.

The thermalized molecules are absorbed by the wall and new molecules are evaporated with Maxwellian velocity distributions, $g(v)$, in the normal (Equation 10) and parallel (Equation 11) directions with reference to the wall. The experimental evidence for the Maxwellian distribution of velocities is given by Loeb [55]. The Maxwell assumption [54] to model the collision of fluid molecules with the wall is based on a hard sphere model. Physically, this assumption allowed the modelling of thermalized post collision velocities using the Maxwellian distribution in both the tangential and normal directions (Equations 10 and 11).

$$g(v)_\perp = \frac{m}{K_b T} \; v \; e^{\left(\frac{-mv^2}{2K_b T}\right)} \tag{10}$$

$$g(v)_\parallel = \sqrt{\frac{m}{2\pi K_b T}} \; e^{\left(\frac{-mv^2}{2K_b T}\right)} \tag{11}$$

Where m is the mass of the molecule, T is the wall temperature and v is the molecular velocity.

Maxwell's coefficient f, has also been referred to as the accommodation coefficient f. In this paper, the effect of surface roughness and the resulting slip or no-slip boundary condition has been approximated with the accommodation coefficient f. A value of $f=1$ corresponds to a no-slip boundary condition, where every molecule that interacts with the wall is thermalized. For $f=0$ none of the molecules that collide with the wall are thermalized.

Arya et al. [56] demonstrated that the accommodation coefficient f is strongly dependent on the physical roughness of the wall (proportional to σ_{wg}/L) and the attractiveness of the wall to the fluid (proportional to ε_{wg}/k_BT) where σ_{wg} and ε_{wg} are the Lennard-Jones interaction parameters of the wall and fluid molecules and L is the lattice unit length. The values of f were also predicted from a molecular boundary.

Sokhan et al. [28] checked the accuracy of Maxwell's theory of slip by analysing the velocity distributions of particles colliding with the wall immediately before and after the collision and did not find any noticeable deviation from the Maxwellian distribution for the tangential component. However, non-Maxwellian behavior was observed for the normal distribution even though it did not induce non-uniformity in the temperature profile. It should, however, be noted that the coefficient f estimated from their simulation was very small ($<= 0.029$).

Molecular velocities given by Equation 2 do not follow a Gaussian distribution for a given temperature value. It was discovered that for large f values, a significant number of molecules received exceptionally high velocities in the normal direction, thereby irreversibly damaging velocity and temperature distributions and making thermostats ineffective. The use of velocity rescaling techniques [57] to maintain constant temperature in the production phase is an over simplification and may not be suitable for accurate prediction of velocity gradients near the wall.

The wall roughness is modelled using an arbitrary parameter f. It is also assumed that the roughness the wall has an influence only on the parallel component of the molecular velocity for the fraction of molecules chosen for the thermalization process. In other words, it is assumed that the wall roughness does not influence the normal component of a chosen colliding molecule. The proposed model is based on the soft sphere collision model given by Hafezi and Ransing [43]. It is argued that the positions of all neighbouring fluid molecules

and wall molecules have an influence on the post collision velocity of a colliding molecule. As a result, it is proposed that the post collision velocity in a normal direction to the wall is conserved for all colliding molecules. In the proposed model, the atomic scale asperities of the larger wall roughness are modelled using high 'f' values thereby thermalizing a larger fraction of the fluid molecules that undergo collision. The soft collision model accounts for the inter-molecular forces between the fluid-fluid and fluid-wall molecules using the Lennard-Jones potential.

2.4 CALCULATION OF THE DRAG FORCE

The stress tensor, calculated at every MLS node, is further averaged using information from the neighbouring nodes near the boundary. An average of the stress tensor values at three MLS nodes is used for the drag force calculations. The numerical integration, as used in Equation 12, assumes a linear variation between two consecutive MLS nodes along the surface. This assumption is computationally efficient but may require a higher density of MLS nodes in areas of higher stress gradients. Figure 4 describes the forces on an element with length L between two MLS nodes. The width in the z direction is given by variable W. A periodic boundary condition was assumed in the z direction. For the given geometries, the normal to the wall is always in the xy plane; the macroscopic velocity in the z direction is zero and hence the stress contribution in the z direction was assumed to be small and is neglected. The ith line segment joining two MLS nodes (MLS^1 and MLS^2) is inclined at an angle θ. Equations 14-19 calculate the elemental forces in the x and y directions. The stress values are parameterised as a variable 't', with t equal to zero 0 at node MLS^1 and t as having unit value at node MLS^2. The resultant drag, or lift force, is calculated by integrating the elemental forces over all line segments (Equations 20).
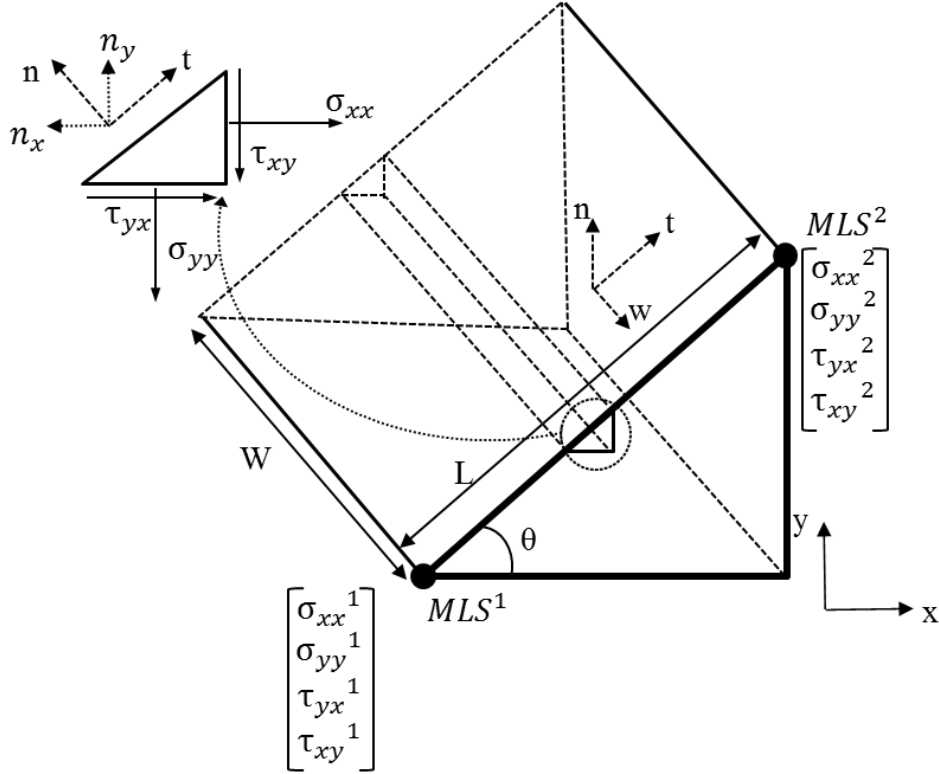
Figure 4. Elemental forces on an ith line segment with length L and width W of a boundary inclined at an angle θ and defined by MLS nodes 1 and 2 (MLS^1 and MLS^2).

$$\vec{F} = \iint_A f \, dA = \iint_A \sigma \cdot \hat{n} \, dA \tag{12}$$

$$f = \begin{bmatrix} f_x \\ f_y \end{bmatrix}_s = \begin{bmatrix} \sigma_{xx} & \tau_{xy} \\ \tau_{yx} & \sigma_{yy} \end{bmatrix} \begin{bmatrix} n_x \\ n_y \end{bmatrix} = \begin{bmatrix} \sigma_{xx} n_x + \tau_{xy} n_y \\ \tau_{yx} n_x + \sigma_{yy} n_y \end{bmatrix} \tag{13}$$

The force acting over the ith line segment of the boundary is:

$$F_x^i = \int_0^W \int_0^L \left(\sigma_{xx}(t) \sin(\theta) + \tau_{yx}(t) \cos(\theta) \right) dt \, dw \tag{14}$$

$$F_y^i = \int_0^W \int_0^L \left(\sigma_{yy}(t) \cos(\theta) + \tau_{xy}(t) \sin(\theta) \right) dl\, dw \qquad (15)$$

$$F_x^i = \int_0^W \left(\frac{\sigma_{xx}^2 - \sigma_{xx}^1}{2L} t^2 + \sigma_{xx}^1 t \right) \sin(\theta) + \left(\frac{\tau_{yx}^2 - \tau_{yx}^1}{2L} t^2 + \tau_{yx}^1 t \right) \cos(\theta) \Bigg|_0^L dw \qquad (16)$$

$$F_y^i = \int_0^W \left(\frac{\sigma_{yy}^2 - \sigma_{yy}^1}{2L} t^2 + \sigma_{yy}^1 t \right) \cos(\theta) + \left(\frac{\tau_{xy}^2 - \tau_{xy}^1}{2L} t^2 + \tau_{xy}^1 t \right) \sin(\theta) \Bigg|_0^L dw \qquad (17)$$

$$F_x^i = W \left(\left(\frac{\sigma_{xx}^1 + \sigma_{xx}^2}{2} \right) L \sin(\theta) + \left(\frac{\tau_{yx}^1 + \tau_{yx}^2}{2} \right) L \cos(\theta) \right) \qquad (18)$$

$$F_y^i = W \left(\left(\frac{\sigma_{yy}^1 + \sigma_{yy}^2}{2} \right) L \cos(\theta) + \left(\frac{\tau_{xy}^1 + \tau_{xy}^2}{2} \right) L \sin(\theta) \right) \qquad (19)$$

The drag and lift forces (F_D and F_L) are obtained by adding forces over all the line segments defining the boundary or the geometry. These values are used in Equation 6 to calculate the drag coefficients.

$$F_D = \sum_{i=1}^k F_x^i \qquad\qquad F_L = \sum_{i=1}^k F_y^i \qquad (20)$$

3 DISCUSSION OF RESULTS

As discussed in Appendix 2, the Knudson number for a methane flow at 300K, 40MPa through an 8.2 nm slit pore is 0.0214. As shown in Figure16, the region of interest for this example is close to the continuum limit.

The simulation is run for three wall geometries: circle, square and diamond shaped cylinders placed inside a slit pore, as tabulated in Figure 5. The depth in the z direction is 8.2 nm for all geometry configurations.
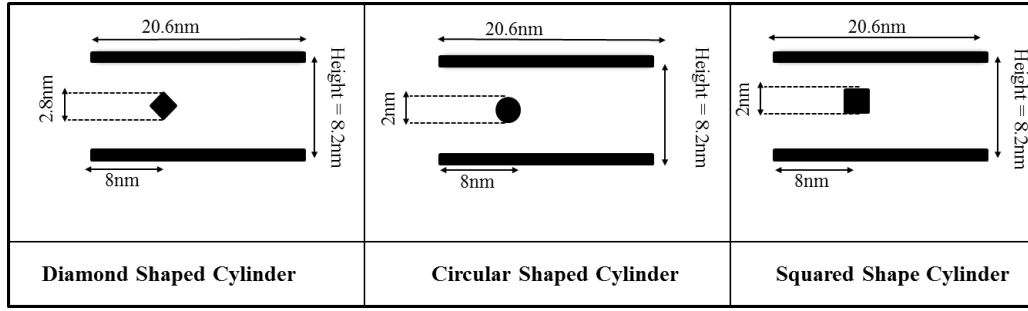
16

Figure 5. Schematic geometries for modelling molecular flow over diamond, circular and square shaped cylinders confined within parallel walls.

The effect of surface roughness as characterized by accommodation coefficient f (0.07, 0.257, 0.45, 0.681 and 1) for various acceleration values (0, 6×10^{11}, 10×10^{11}, 50×10^{11}, 100×10^{11} (m/s^2)) is discussed for all three geometries.

The Reynolds numbers for the slit pore flow over a cylinder are calculated from the overall macroscopic velocity for a given surface roughness and acceleration value. For example, assuming a surface roughness, f, value of one and the acceleration value of 10 m/s^2, the overall macroscopic velocity, for the circular shaped cylinder, is calculated as 74 m/s. Further assuming a constant value for kinematic viscosity of methane as 1.1868E^{-7}(m^2/s) and using the diameter of the cylinder as characteristic length, the Reynolds number for flow over the cylinder is calculated as 1.25.

3.1 VERIFICATION OF PRESSURE CALCULATIONS

The number density of molecules is calculated for a temperature and pressure value of 300K and 40MPa respectively (Appendix 2). Using this density a simulation with 5140 molecules was undertaken for a periodic boundary condition in all three directions with no walls. The pressure value was calculated using the following approximate equations.

The Irwin-Kirkwood method (Equation 7) ignores the long correction W_{LR}. The long range correction to the pressure value is constant for a given cut off radius, fluid molecules and number of molecules [58] and is given by Equation 23. The non-inclusions of the long range correction factor for calculating forces around an object may be justified as its effect will get cancelled during the cyclic integral of the stress tensor. The kinetic part is calculated using

the average temperature and the configurational part ignored the correction term l_{ij} as discussed in the previous section but instead used the neighbourhood list for each molecule to decide the contribution from intermolecular forces.

$$P = \rho\left(K_b T - \frac{W}{3N}\right) = \rho\left(K_b T - \frac{W_{SR}}{3N} - \frac{W_{LR}}{3N}\right) \tag{21}$$

$$W_{SR} = \sum_{i=1}^{N-1}\sum_{j>i}^{N}\left[F_{LJ,ij} \cdot \left(\frac{r_{ij}^2}{r_{ij}}\right)\right] \tag{22}$$

$$W_{LR} = -\frac{1}{2}\frac{N^2}{V}\left[\frac{96\pi\varepsilon}{9}\left(2\frac{\sigma^{12}}{r_{cut}^9} - 3\frac{\sigma^6}{r_{cut}^3}\right)\right] \tag{23}$$

The average pressure at all MLS nodes in the domain was calculated as 39.23 MPa. This value is within 2% of the assumed 40MPa value. In addition to this, the instantaneous molecular velocity distributions in the x, y and z directions were compared with the Gaussian distributions corresponding to its temperature value and a close agreement was observed.

3.2 FLOW PAST A SQUARE CYLINDER FOR CONTINUUM AND MOLECULAR WALLS

Hafezi and Ransing [43] showed that the equivalent positions of molecules around the molecular and an equivalent continuum wall are not identical. The calculations illustrated that the molecules could be up to 0.2 Angstrom closer to the molecular wall than the equivalent continuum wall. However, the results did not show the appreciable impact on the average velocity distribution.

The results from the molecular and continuum wall models are compared. In this simulation, the velocity in the z direction is ignored from calculations for the average two dimensional velocities at MLS nodes. Even though the resulting velocity profiles were similar, the magnitudes of pressure values were different for both continuum and molecular walls. As a result, simulations were undertaken for a molecular square cylinder in a molecular slit pore and compared with an equivalent continuum wall. It was found that the continuum wall predicted pressure values up to 20% higher than the molecular wall for various acceleration values. However, the resulting drag coefficient variations with respect to Reynolds number

were very similar (Figure 6). The simulation time required for the continuum wall was at least four times smaller than for the equivalent molecular wall. As a result, the rest of the simulations were undertaken on using continuum walls for the cylinder and the slit pore. It is also noted that the continuum wall assumptions will allow inputting experimentally determined forces to the simulation. It is assumed that in future the experimental research community will be able to measure such nanoscale forces under various practical conditions.
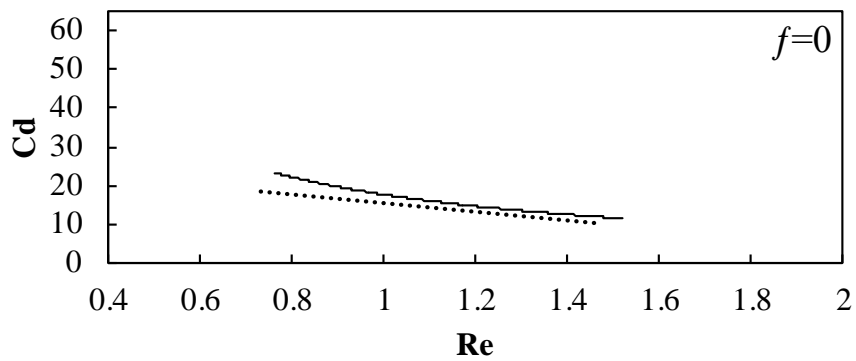
$f=0$

$f=0.257$

$f=1$
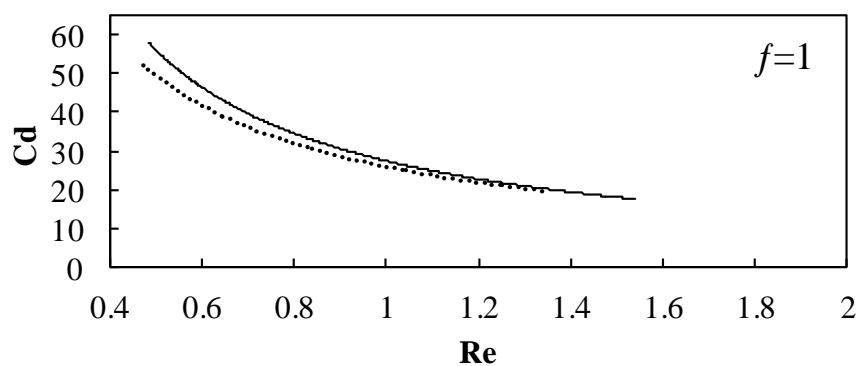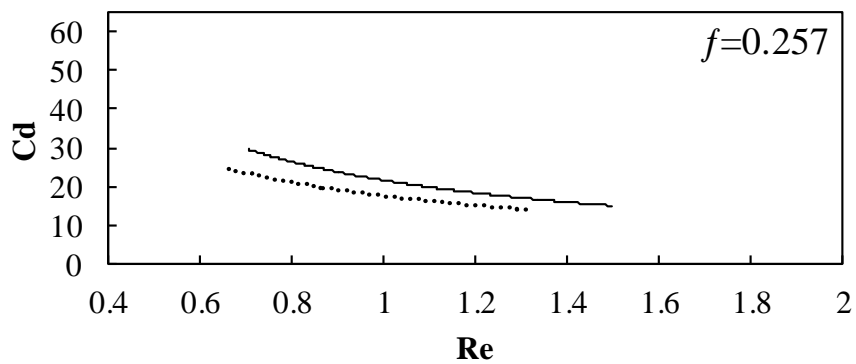
Figure 6. Comparison of drag coefficient variation with respect to Reynolds numbers using molecular (dotted curve) and continuum wall (continuous curve) assumptions.

3.3 COMPARISON OF PREDICTED DRAG COEFFICIENT VALUES WITH CONTINUUM BASED METHODS AND ANALYTICAL SOLUTIONS

For molecular flow at a nanoscale slit pore, the inertial forces are much smaller than the viscous forces thereby making the Reynolds number (Re) value much less than unity. Purcell [59], Squires and Quake [60] have reported occasional 'counter intuitive' results for molecular flows at very low Reynolds numbers.

The predicted drag coefficient values for a smooth circular cylinder ($f = 0$) are compared with the analytical solution derived from the continuum calculations [61] (Figure 7). The predicted values by the proposed formulation are five to seven times higher than the ones determined from a continuum based analytical solution. The corresponding pressure contours are shown in Appendix 1 for various acceleration values. It is observed that the wall did not interfere with the pressure gradients around the cylinder for acceleration values up to 50 m/s^2 or Reynolds number values up to 1.5. Hence, the predicted drag coefficient values are compared with the drag values for uniform flow over a cylinder. Tang and Advani [62] have calculated drag on a nanotube in an uniform argon flow. They have observed a similar trend that continuum based techniques underestimated the drag coefficients as compared to the molecular dynamics simulations for Reynolds number less than unity (Figure 7). However, the predicted drag coefficient values from the proposed formulation are 20-40% higher than the ones calculated by Tang and Advani [62]. One of the reasons could be that they calculated the instantaneous force on the nanotube at each time step by summing up the forces on all the carbon nano-tube atoms. The time average values estimated the average drag force. The proposed formulation calculates localised macroscopic stress tensor values and then constructs the resulting force value. This allows an extension of the methodology to model the flow over complex geometries and estimating the resulting drag coefficients.

The horizontal error bars in Figure 7 illustrate the variation in the average velocity values

20

calculated at every 0.2 ns. A sample calculation showing the variation in x and y components of average velocity values is shown in Figure 9 by dotted curves. A Reynolds number value of 1.8, molecular acceleration value 50 m/s^2 and surface roughness value 1 is used for these calculations. The detailed procedure is described in Section 2.2. The corresponding geometry and the positions (position 1, p1 and position 2, p2) at which the velocity contours are plotted is shown in Figure8. The variation in the z direction appears large, however, the magnitude is close to zero as the z direction has a periodic boundary condition and there is no average flow in the z direction. However, the observed negative velocities are attributed to molecular interaction and collisions as the simulation is in three dimensions. The stress tensor in Equations 2 and 13 is two dimensional and the variation in the corresponding stress values is shown in Figure 10. This variation is much smaller than the variation observed for the velocity values as the local average velocity values at the corresponding time steps were used in Equation 10. Hence, the error bars shown on the drag coefficient values in Figure 7 are estimated to be significantly smaller than the error bars for the Reynolds number.
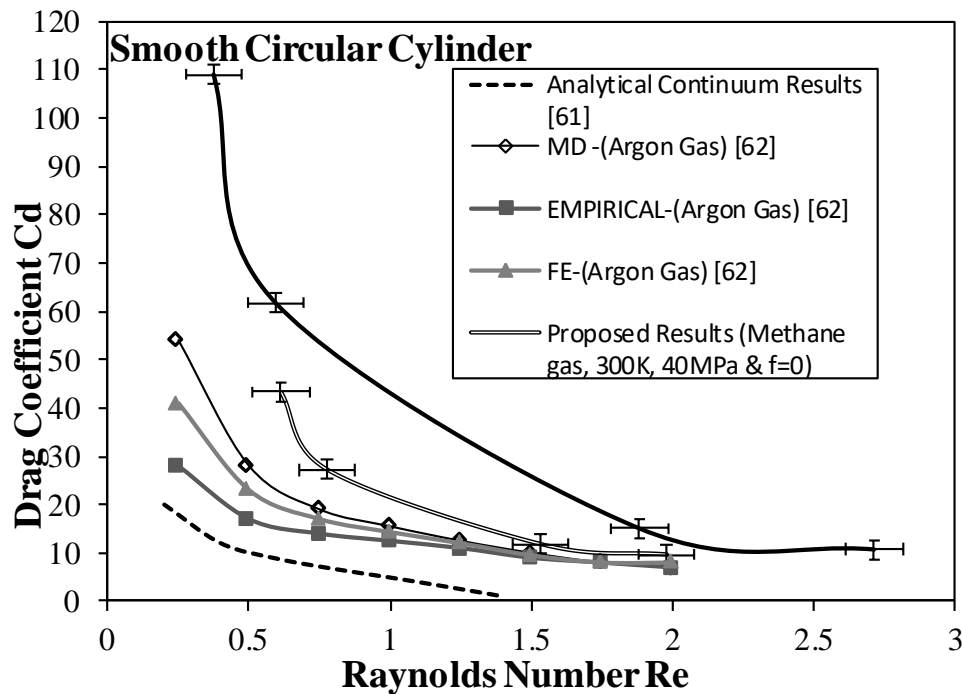

Figure 7. Comparison of drag coefficient variation with Reynolds number for the proposed molecular dynamics simulation with continuum based analytical solutions [61]. The horizontal error bars on the proposed results show sensitivity to 15% variation in the assumed kinematic viscosity value and the vertical error bars relate to the molecular variation in the average velocity value.
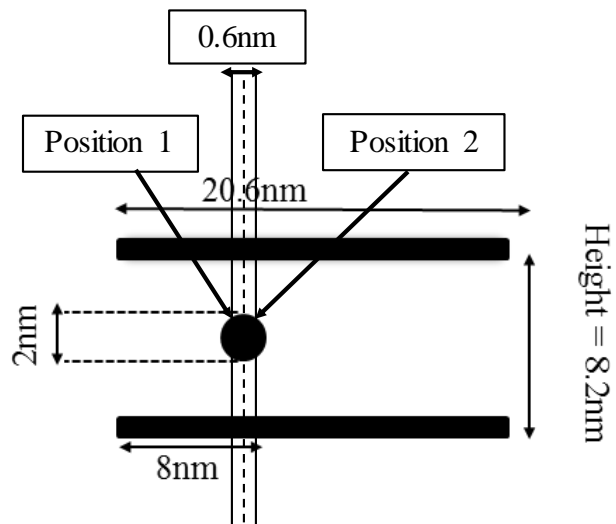
Figure 8: The positions 1 and 2 are shown on the schematic geometry. The average contour values in Figure are shown at these positions (p1 and p2).
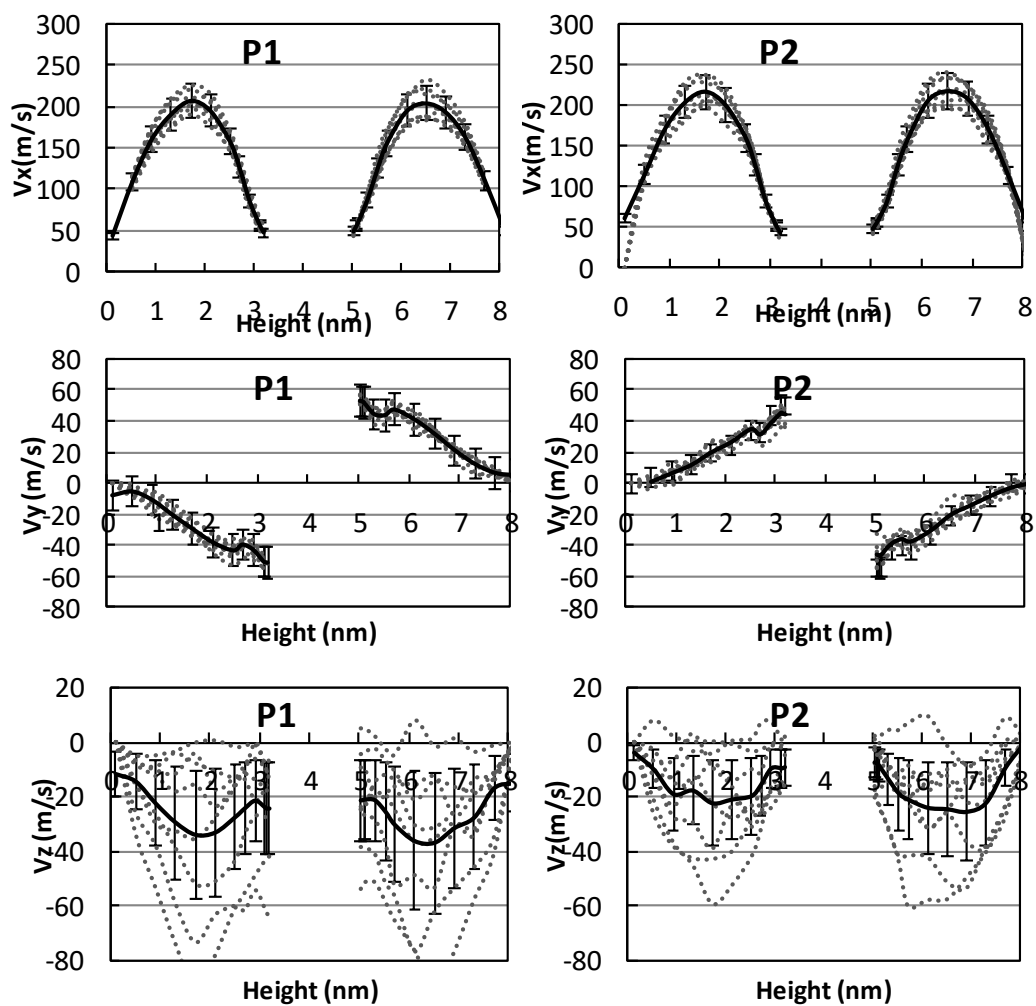
Figure 9: Variation in average velocity contours calculated at every 0.02ns (dotted curve) at positions 1 and 2 as shown in Figure 8.
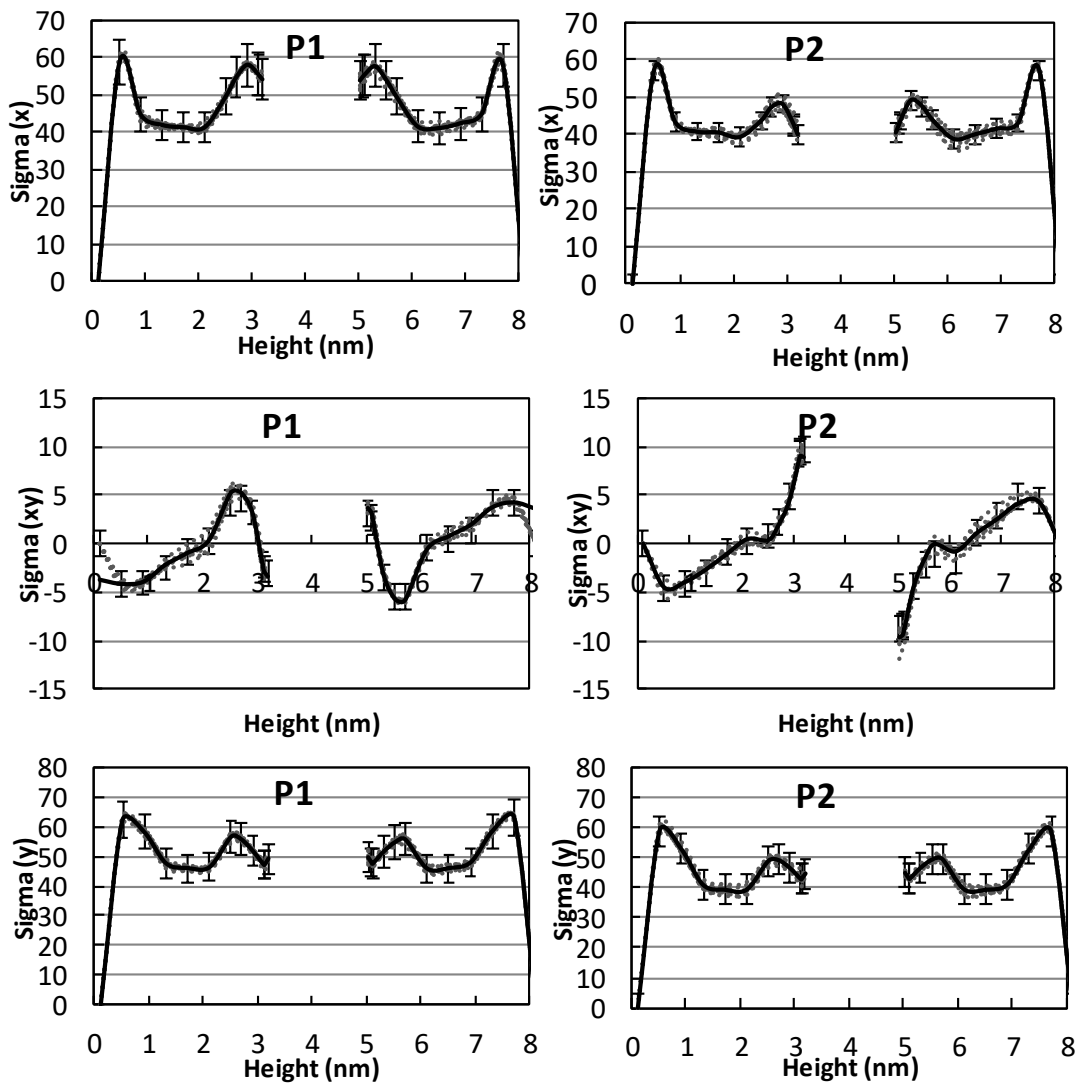
Figure 10: Variation in average stress values calculated at every 0.02ns (dotted curve) at positions 1 and 2 as shown in Figure 8.

3.4 SUMMARY OF RESULTS

The graphs describing the variation of drag coefficient with respect to Reynolds number for various surface roughness values (f = 0, 0.07, 0.257, 0.45, 0.681 and 1) are shown in Figures 11, 12 and 13 for diamond, cylinder and square cylinders respectively. It is shown that for a given Reynolds number, the drag coefficient increases with the surface roughness for all cylindrical geometries. It is also observed that the drag coefficient reduces with an increase in the Reynolds number value for all cases.
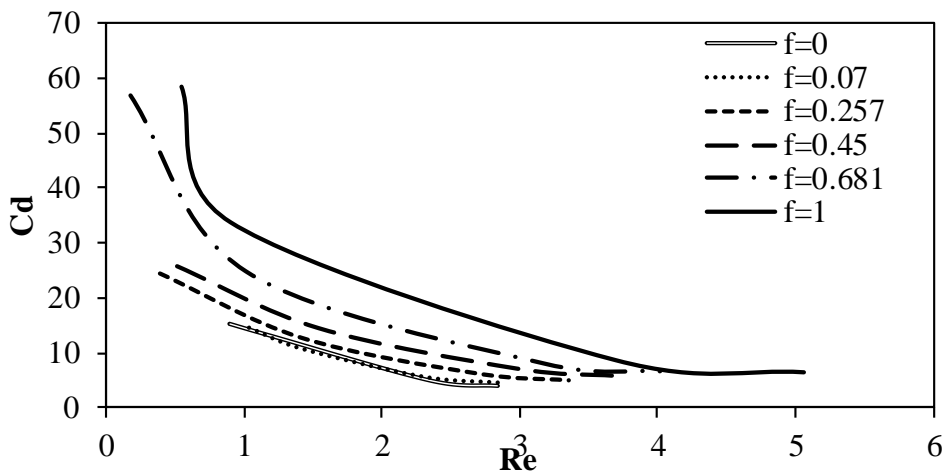

Figure 11. Drag coefficient variation with respect to Reynolds number for different roughness values for molecular flow over a diamond shaped cylinder within a slit pore with continuum wall assumptions.
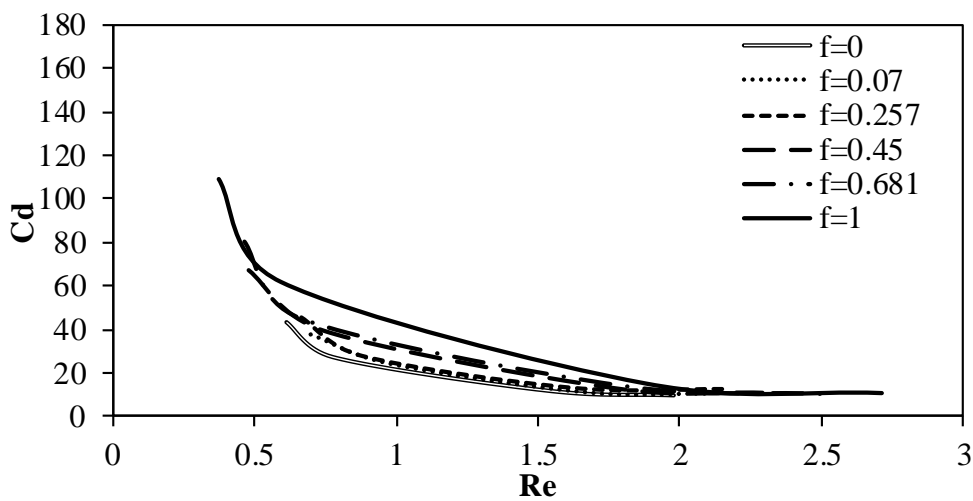
Figure 12. Drag coefficient variation with respect to Reynolds number for different roughness values for molecular flow over a circular shaped cylinder within a slit pore with continuum wall assumptions.
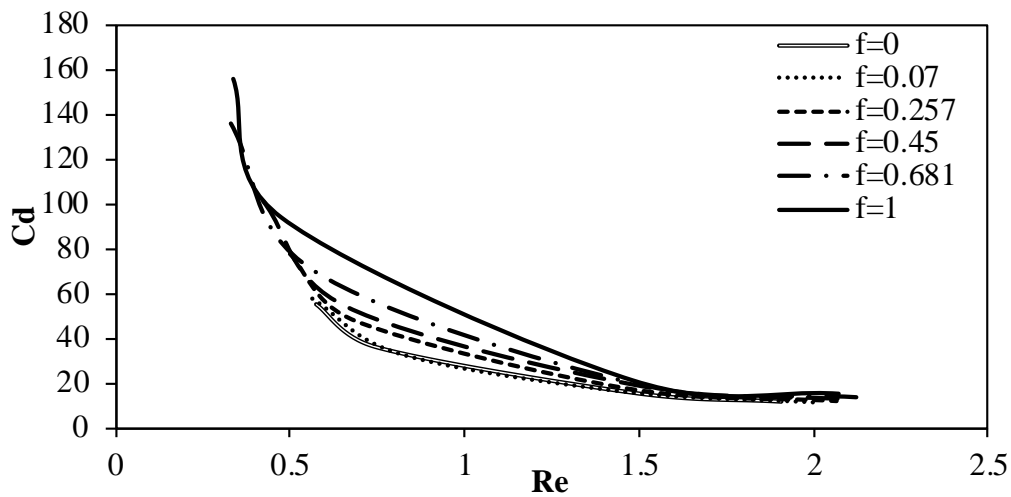

Figure 13. Drag coefficient variation with respect to Reynolds number for different roughness values for molecular flow over a square cylinder within a slit pore with continuum wall assumptions.

Figure 14 groups the variation of drag coefficients with respect to Reynolds number for the three cylindrical shapes and plots the corresponding graphs for each surface roughness value. It is observed that the drag is a minimum for the flow over a diamond shaped cylinder and a maximum for the square shaped cylinder.
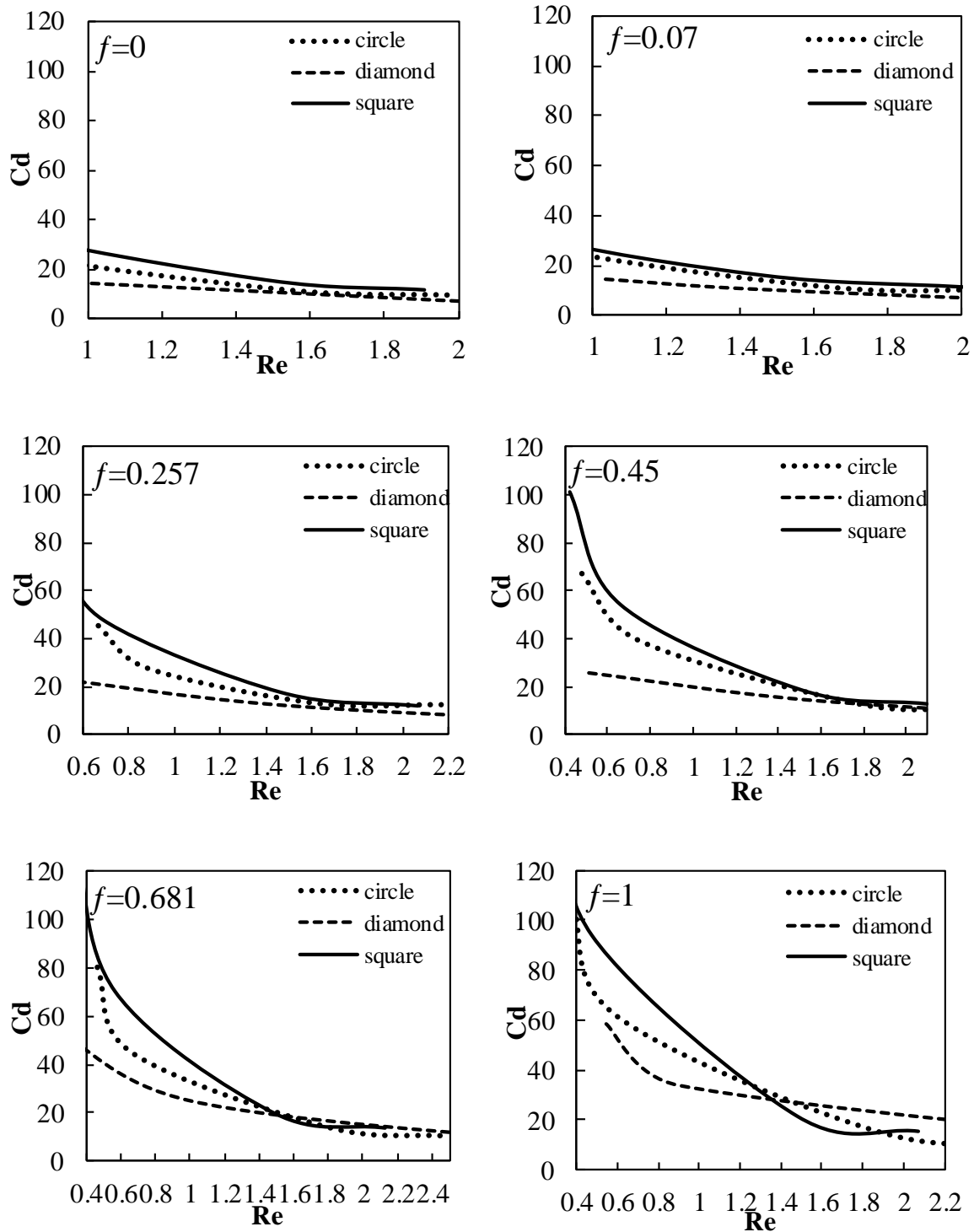
Figure 14. Drag coefficient variation with respect to Reynolds number for circular, diamond and square shaped cylinders. The graphs are shown for different surface roughness values.

4 CONCLUSIONS

A detailed mathematical formulation, based on first principles, is proposed to predict drag coefficients for a molecular flow over nano sized bodies or devices. The drag coefficient variation with respect to Reynolds numbers, under various conditions such as cylinder shape and surface roughness, is studied for low Knudson number flows that are close to the continuum limit.

The pressure and streaming velocity values are calculated at given MLS nodes within the computational domain. The nodal density is user defined and it allows calculation of pressure variation over complex shaped geometries, including three dimensional bodies. It was noted that attaching molecular structures on the wall was not a correct representation of wall roughness as continuum wall dimensions approach to submicron or nanoscale. The slip effect due to surface roughness at the continuum wall is, instead, modelled using an accommodation coefficient f. It was discovered that pressure calculations are sensitive to the molecular or continuum wall assumptions and up to 20% variation was observed. However, the difference in the force values was approximately constant and hence, the resulting drag coefficient values remained within 2-15%. The maximum error occurred at very low Reynolds numbers (~0.5).

It has been shown that the existing molecular dynamics, or continuum based, approaches underestimate nanoscale drag coefficients by at least 20-40%. These coefficients are also up to seven times higher than the ones calculated by continuum based analytical solutions. The magnitude of underestimation increases as the Reynolds number value is lowered from one.

APPENDIX 1: Pressure contours for flow past a circular shaped smooth cylinder with continuum wall assumptions.
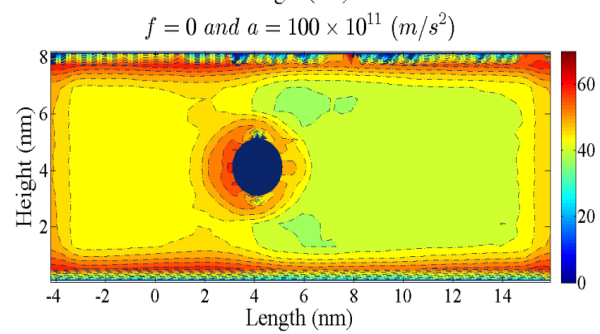

$f = 0$ and $a = 0 \times 10^{11}$ (m/s^2)

$f = 0$ and $a = 6 \times 10^{11}$ (m/s^2)

$f = 0$ and $a = 10 \times 10^{11}$ (m/s^2)

$f = 0$ and $a = 50 \times 10^{11}$ (m/s^2)
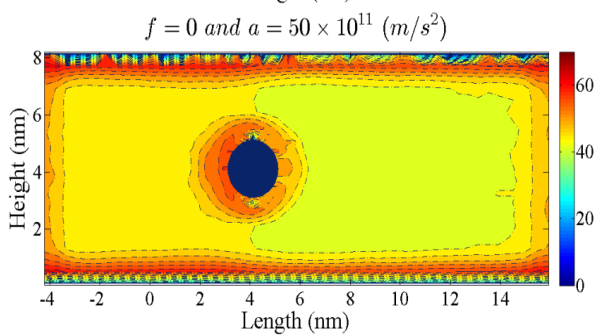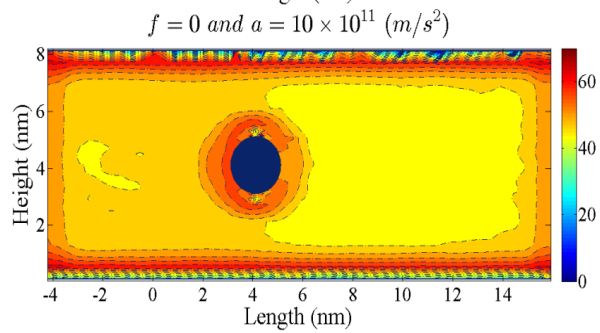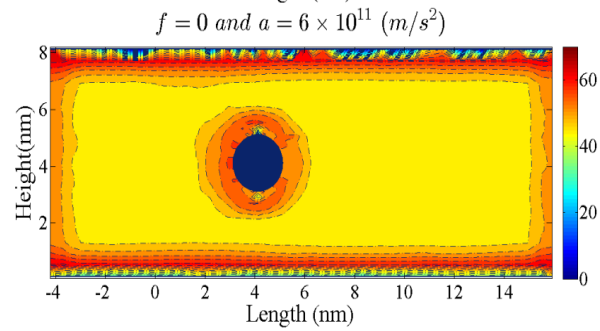
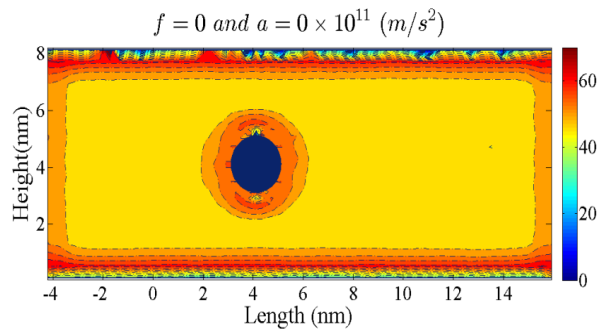$f = 0$ and $a = 100 \times 10^{11}$ (m/s^2)

Figure 15. Pressure contours for flow past a circular shaped smooth cylinder (f=0) and molecular accelerations value 0, 6,10,50,100 (m/s^2)

APPENDIX 2: Continuum Limit and Calculation of Molecular Volume For Methane At 40MPa And 300K From First Principles

Using the kinetic theory of gases, the mean free path for methane gas is proportional to $\frac{1}{na^2}$ where n is the number density of molecules with a radius 'a'. The gas is characterized as dilute gas if $\delta/d \gg 1$, where d is the molecular diameter and δ is the average molecular spacing. Squires and Quake [60] have reported a mean free path for air molecules as 70 nm at 1atm and 25°C. This means that for an understanding of the interaction of air with a boundary at dimensions around 70nm, the contributions from molecular dynamics cannot be ignored. Schaaf and Chambre [63] classified different flow regimes based on the Knudsen number. Fluid is considered as continuum for Kn <= 0.01 and the assumption of a no-slip boundary condition at the fluid-wall interface remains valid. The flow between Kn >0.01 and Kn < 0.1 is categorized as slip flow which then becomes transitional flow up to Kn =10. For Kn > 10 the flow is considered as a free molecular flow. Karniadakis et al. [64] have further classified this range and introduced a region (Figure 16) where statistical fluctuations due to molecular contributions are assumed to be greater than 1%. This region is classified by a line with L/δ ratio equal to 20. Where, L is the characteristic length.
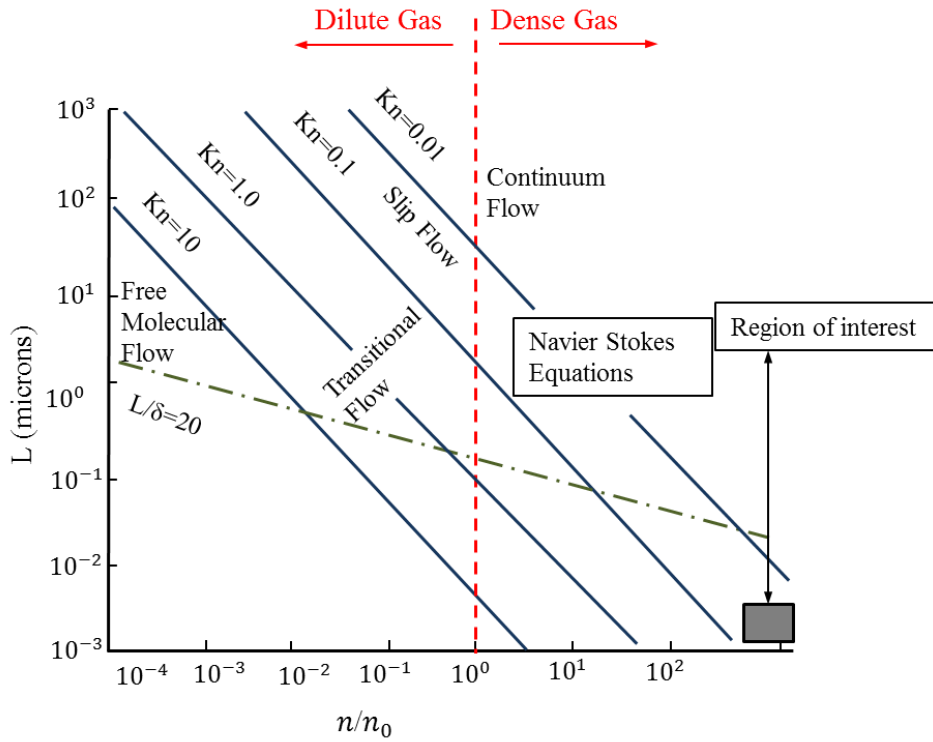
Figure 16. Limits of approximations in modelling gas microflows [64]. n/n_0 is the number density normalized with corresponding atmospheric conditions. L is the characteristic length. Kn is Knudsen number and δ is the mean molecular spacing

The location of the region of interest, shown as a square in Figure 16, is calculated as follows:

For methane gas at 40MPa and 300K, the number density is calculated using the perfect gas equation:

$$\frac{1}{V} = \frac{P}{zR_uT} = \frac{P}{zN_AK_BT} = \frac{n}{N_A} \tag{24}$$

$$n = \frac{P}{zK_BT} \qquad (A^\circ)^3 \tag{25}$$

Where:

P : Gas pressure (Pa)

z : Compressibility factor

T: Temperature (K)

N_A: Avogadro's number

R_u: Universal gas constant

K_B: Boltzmann constant

n: Number density

The compressibility factor for methane at 40MPa and 300K is determined using compressibility charts [65]. This requires calculation of reduced pressure P_R and temperature T_R values that are based on the critical pressure P_{cr} and temperature T_{cr} values.

$$P_R = \frac{P}{P_{cr}} = \frac{400}{45.99} \approx 8.77 \qquad (26)$$

$$T_R = \frac{T}{T_{cr}} = \frac{300}{274.14 - 82.59} = 1.566 \qquad (27)$$

the compressibility factor z is assumed as 1.06

Using Equation 31, the number density n is calculated as follows:

$$n = \frac{P}{zK_B T} = \frac{40 \times 10^6}{1.06 \times 1.38 \times 10^{-23} \times 300} = 9.11926 \times 10^{27} \ (A^\circ)^3$$

The volume occupied by each methane molecule is 1/n and a value of 109.66 $(A^\circ)^{-3}$ has been used in this paper to correspond with a temperature and pressure value of 300K and 40MPa.

Hence,

$$n_0 = \frac{P_0}{zK_B T_0} \ (A^\circ)^3$$

$$\frac{n}{n_0} = \frac{9.1192 \times 10^{27}}{2.69 \times 10^{25}} \approx 339$$

The width L of the slit pore is $L = 8.24 \times 10^{-9}$ (m)

The Knudsen number is calculated as follows:

The molecular diameter (d) of methane is calculated using a critical volume value for methane as 99 (cc/mol) [66] using the following equation

$$d = 0.8094 V_c^{1/3} \tag{28}$$

$$d = 3.742 \times 10^{-10} \text{(m)}$$

$$L = 8.24 \times 10^{-9} \text{(m)}$$

The mean free path λ is given by:

$$\lambda = \frac{1}{\sqrt{2}\pi d^2 n} = \frac{1}{\sqrt{2} \times \pi \times (3.742 \times 10^{-10})^2 \times 9.11926 \times 10^{27}} = 1.7627 \times 10^{-10} \text{(m)} \tag{29}$$

And, hence the Knudsen number is given by:

$$K_n = \frac{\lambda}{L} = \frac{1.7627 \times 10^{-10}}{8.24 \times \times 10^{-9}} = 0.0214 \tag{30}$$

The L/ δ ratio, where $\delta \propto \dfrac{1}{\sqrt[3]{n}}$ this ratio is less than 20 and hence, as shown in Figure , it is expected that molecular contributions should be significant even if the Knudsen number close to the continuum limit of 0.01.

REFERENCES

1. Turgeon ML. *Clinical Hematology Theory and Procedures*, Lippincott Williams & Wilkins 2005

2. Berg HC *E. Coli in Motion*, Springer-Verlag New York 2004.

3. Mandelkern M, Elias, JG, Eden, D & Crothers DM. The dimensions of DNA in solution. *Journal of Molecular Biology* 1981; **152,** 153-16.

4. Bawa R. Nanoparticle-based Therapeutics in Humans: A Survey. *Nanotechnology Law & Business* 2008 ; **5,** 135-155.

5. World C., Garin G. & Berk B. Vascular shear stress and activation of inflammatory genes. *Current Atherosclerosis Reports* 2006; **8,** 240-244.

6. Bean AJ *Protein Trafficking in Neurons*, Elsevier Science, 2006.

7. Howard J. *Mechanics of Motor Proteins and the Cytoskeleton*, Sinauer Associates, Incorporated, 2001.

8. Hess H. & Vogel V. Molecular shuttles based on motor proteins: active transport in synthetic environments. *J Biotechnol* 2001; **82,** 67-85.

9. Kipp JE. The role of solid nanoparticle technology in the parenteral delivery of poorly water-soluble drugs. *International Journal of Pharmaceutics* 2004; **284,** 109-122.

10. Ould-ouali L., Noppe M., Langlois X., Willems B., Te-riele P., Timmerman, P., Brewster ME, Ariën A & Préat V. Self-assembling PEG-p(CL-co-TMC) copolymers for oral delivery of poorly water-soluble drugs: a case study with risperidone. *Journal of Controlled Release* 2005; **102,** 657-668.

11. Suri SS, Fenniri H. & Singh B. Nanotechnology-based drug delivery systems. *J Occup Med Toxicol* 2007; **2,** 16.

12. Groneberg DA, Rabe KF & Fischer A. Novel concepts of neuropeptide-based drug therapy: Vasoactive intestinal polypeptide and its receptors. *European Journal of Pharmacology* 2006; **533,** 182-194.

13. Tan J, Shah S, Thomas A, Ou-yang HD & Liu Y. The influence of size, shape and vessel geometry on nanoparticle distribution. *Microfluid Nanofluidics* 2013; **14,** 77-87.

14. Kingsley JD, Dou H, Morehead J, Rabinow B, Gendelman HE & Destache CJ. Nanotechnology: a focus on nanoparticles as a drug delivery system. *J Neuroimmune Pharmacol* 2006; **1,** 340-50.

15. Uhrich KE, Cannizzaro SM, Langer RS & Shakesheff KM. Polymeric systems for controlled drug release. *Chem Rev* 1999; **99,** 3181-98.

16. Arruebo M, Fernández-pacheco R, Ibarra MR & Santamaría J. Magnetic nanoparticles for drug delivery. *Nano Today* 2007; **2,** 22-32.

17. Dobson J. Magnetic micro- and nano-particle-based targeting for drug and gene delivery. *Nanomedicine* 2006; **1,** 31-37.

18. Misra RDK. Magnetic nanoparticle carrier for targeted drug delivery: perspective, outlook and design. *Materials Science and Technology* 2008; **24,** 1011-1019.

19. Vartholomeos P. & Mavroidis C. Simulation platform for self-assembly structures in MRI-guided nanorobotic drug delivery systems. *In:* Robotics and Automation (ICRA), 2010 IEEE International Conference on, 3-7 May 2010. 5594-5600.

20. Vartholomeos P, Fruchard M, Ferreira A. & Mavroidis C. MRI-guided nanorobotic systems for therapeutic and diagnostic applications. *Annu Rev Biomed Eng* 2011; **13,** 157-84.

21. Gupta RB. & Kompella UB. *Nanoparticle Technology for Drug Delivery*, Taylor & Francis, 2006.

22. Sirk T. *Numerical Simulation of Nanoscale Flow: A Molecular Dynamics Study of Drag.* MS Thesis, Virginia Polytechnic Institute and State University USA, 2006.

23. Gijs MM Magnetic bead handling on-chip: new opportunities for analytical applications. *Microfluidics and Nanofluidics* 2004; **1,** 22-40

24. Ahmadi G. & Guo S. Bumpy Particle Adhesion and Removal in Turbulent Flows Including Electrostatic and Capillary Forces. *The Journal of Adhesion* 2007; **83,** 289-311.

25. Huang C, Choi PY, Nandakumar K. & Kostiuk LW. Investigation of entrance and exit effects on liquid transport through a cylindrical nanopore. *Phys Chem Chem Phys* 2008; **10,** 186-92.

26. Bhushan B. Nanotribology and nanomechanics of MEMS/NEMS and BioMEMS/BioNEMS materials and devices. *Microelectronic Engineering* 2007; **84,** 387-412.

27. Dyson P, Ransing RS, Williams PH. & Williams R. *Fluid Properties at Nano-meso Scale: A Numerical Treatment.*Wiley, 2008. ISBN 978-0-470-75124-4.

28. Sokhan VP, Nicholson D. & Quirke N. Fluid flow in nanopores: An examination of hydrodynamic boundary conditions. *The Journal of Chemical Physics* 2001; **115,** 3878-3887

29. Adisa, O. O. *Modelling gas storage in molecular nanosystems.* PhD Thesis, The University of Adelaide, Australia, 2012.

30. Volkova EI, Suyetin MV & Vakhrushev AV. Temperature Sensitive Nanocapsule of Complex Structural Form for Methane Storage. *Nanoscale Research Letters* 2009; **5,** 205-210.

31. Lees AW, & Edwards SF. The computer study of transport processes under extreme conditions. *Journal of Physics C: Solid State Physics* 1972; **5,** 1921.

32. Barisik M. & Beskok A. Equilibrium molecular dynamics studies on nanoscale-confined fluids. *Microfluidics and Nanofluidics* 2011*,* **11,** 269-282.

33. To QD, Pham TT, Lauriat G. & Léonard C. Molecular Dynamics Simulations of Pressure-Driven Flows and Comparison with Acceleration-Driven Flows. *Advances in Mechanical Engineering,* 2012**;** article id 580763.

34. Asiteropoulou D, Karakasidis TE & Liakopoulos A. Dissipative Particle Dynamics investigation of parameters affecting planar nanochannel flows. *Materials Science and Engineering: B* 2011; **176,** 1574-1579.

35. Kasiteropoulou D, Karakasidis TE & Liakopoulos A. A dissipative particle dynamics study of flow in periodically grooved nanochannels. *International Journal for Numerical Methods in Fluids* 2012; **68,** 1156-1172.

36. Hilbers PAJ, Nedea SV, Markvoort AJ, Ten Eikelder HMM & Spijker P. Implicit particle wall boundary condition in molecular dynamics. *Proceedings of the Institution of Mechanical Engineers, Part C: Journal of Mechanical Engineering Science* 2008; **222,** 855-864.

37. Jabbarzadeh A. Molecular Dynamics Simulations of Flow over a Nano-cylinder in a Rectangular Nano-channel *NANOTECH* 2010; **2,** 733-736.

38. Fan X-J, Phan-thien N, Yong NT & Diao X. Molecular dynamics simulation of a liquid in a complex nano channel flow. *Physics of Fluids* 2002; **14,** 1146-1153.

39. Irving JH & Kirkwood JG. The Statistical Mechanical Theory of Transport Processes. IV. The Equations of Hydrodynamics. *The Journal of Chemical Physics* 1950; **18,** 817-829.

40. Sofos F, Karakasidis TE & Liakopoulos A. Effect of wall roughness on shear viscosity and diffusion in nanochannels. *International Journal of Heat and Mass Transfer* 2010; **53,** 3839-3846.

41. Nagayama G. & Cheng P. Effects of interface wettability on microscale flow by molecular dynamics simulation. *International Journal of Heat and Mass Transfer* 2004; **47,** 501-513.

42. Lion TW & Allen RJ Computing the local pressure in molecular dynamics simulations. *J Phys Condens Matter* 2012; **24,** 0953-8984.

43. Hafezi F and Ransing RS. Computational modelling of fluid structure interaction at nano-scale boundaries with modified Maxwellian velocity distribution. *Applied Mathematical Modelling* 2013; **37**, 7504-7520.

44. Hartkamp R, Ghosh A, Weinhart T & Luding S. A study of the anisotropy of stress in a fluid confined in a nanochannel. *J Chem Phys* 2012; **137,** 4737927.

45. Lauga E, Brenner M and Stone HA. Microfluidics: The No-Slip Boundary Condition. Ch 15 Handbook of Experimental Fluid Dynamics, Editors J Foss, C Tropea and A Yarin, Springer, New York 2005.

46. Mickel W, Joly L. & Biben T. Transport, phase transitions, and wetting in micro/nanochannels: A phase field/DDFT approach. *The Journal of Chemical Physics* 2011; **134,** 094105.

47. Basagaoglu H. & Succi S. Lattice-Boltzmann simulations of repulsive particle-particle and particle-wall interactions: coughing and choking. *J Chem Phys* 2010; **132,** 3374685.

48. Zhang H, Zhang Z. & Ye H. Molecular dynamics-based prediction of boundary slip of fluids in nanochannels. *Microfluidics and Nanofluidics* 2011; **12,** 107-115

49. Li Y, Xu J. & Li D. Molecular dynamics simulation of nanoscale liquid flows. *Microfluidics and Nanofluidics* 2010; **9,** 1011-1031.

50. Yang SC. Effects of surface roughness and interface wettability on nanoscale flow in a nanochannel. *Microfluidics and Nanofluidics* 2006; **2,** 501-511.

51. Sofos F, Karakasidis T. & Liakopoulos A. Surface wettability effects on flow in rough wall nanochannels. *Microfluidics and Nanofluidics* 2012; **12,** 25-31.

52. Sun J, He Y, Tao W, Yin X & Wang H. Roughness effect on flow and thermal boundaries in microchannel/nanochannel flow using molecular dynamics-continuum hybrid simulation. *International Journal for Numerical Methods in Engineering* 2012; **89,** 2-19.

53. Liang Y, Hilal N, Langston P. & Starov VM. Interaction forces between colloidal particles in liquid: Theory and experiment. *Advances in colloid and Interface Science* 2007; **134**, 151-157.

54. Maxwell JC. On Stresses in Rarefied Gases Arising from Inequalities of Temperature. *Proceedings of the Royal Society of London* 1878; **27,** 304-308.

55. Loeb LB *The Kinetic Theory of Gases* New York, Corier Dover Publications, 2004.

56. Arya G, Chang H-C. & Maginn EJ. Molecular Simulations of Knudsen Wall-slip: Effect of Wall Morphology. *Molecular Simulation* 2003; **29,** 697-709.

57. Toghraie Semiromi D. & Azimian AR. Nanoscale Poiseuille flow and effects of modified Lennard–Jones potential function. *Heat and Mass Transfer* 2010; **46,** 791-801.

58. Frenkel D. & Smit, B. *Understanding Molecular Simulation: From Algorithms to Applications*, Elsevier Science, 2001.

59. Purcell EM. Life at Low Reynolds Number. *American Journal of Physics* 1977; **45,** 3-11.

60. Squires TM & Quake SR. Microfluidics: Fluid physics at the nanoliter scale. *Reviews of Modern Physics* 2005; **77,** 977-1026.

61. Lagree, P. Y. *Small Re flows* [Online]. Paris: Institut Jean Le Rond Alembert, 2013. Available: http://www.lmm.jussieu.fr/~lagree/COURS/M2MHP/petitRe.pdf [Accessed 30th October 2015].

62. Tang W and Advani S.G. Drag on nanotube in uniform liquid argon flow. *The Journal of Chemical Physics* 2006; **125**, 174706.

63. Schaaf SA & Chambre PL *Flow of Rarefied Gases*, Princeton University Press, 1961.

64. Karniadakis G, Besko A. & Aluru N. *Microflows and Nanoflows: Fundamentals and Simulation*, Springer. 2005.

65. http://www.reviewpe.net/penotes/thermo/fig_2.01.jpg [Accessed 30th October 2015].

66. Dutta, A. *Multicomponent Gas Diffusion And Adsorption In Coals For Enhanced Methane Recovery.* MSc thesis, Stanford University, 2009.

Table 1. Review of various approaches for calculating the kinetic and configurational part of the Irwin-Kirkwood expression.

Kinetic part: $\sigma_{\alpha\beta}^{K}(r)$	Configuration part: $\sigma_{\alpha\beta}^{U}(r)$	Streaming Velocity
(1) $\dfrac{1}{V}\sum_{i}^{N} m_i u_{i\alpha} u_{i\beta}$ m_i: atomic mass α and β: coordination system axes which for Cartesian system can be simply X,Y and Z $u_{i\alpha}, u_{i\beta}$: the peculiar velocity components of particle i in the α and β directions.	$\dfrac{1}{V}\sum_{i}^{N}\sum_{j>i}^{N} r_{ij\alpha} F_{ij\beta}$ $r_{ij\alpha}$: α component of the distance vector between particle i and j $F_{ij\beta}$: β component of the force exerted on particle i by particle j	$U_{x,b} = \dfrac{\sum\limits_{i=1}^{N_b} m_i v_{i,x}}{\sum\limits_{i=1}^{N_b} m_i}$ m_i, v_i: mass and velocity of atom i inside the bin N_b: number of atoms inside the bin
(2) $\dfrac{1}{3\Omega}\dfrac{|p_i|^2}{m_i}\Lambda_i$ Ω: volume of the region of interest Λ_i: unity if particle i lies within the volume Ω, and zero otherwise	$\dfrac{1}{3\Omega}\cdot\sum_{i=1}^{N-1}\sum_{j>i}(\vec{r_i}\cdot\vec{F_{ij}})l_{ij}$ $\vec{r_i}$ and $\vec{r_j}$: positions of particles i and j $\vec{r_{ij}}=\vec{r_i}-\vec{r_j}$ $\vec{F_{ij}}$: force exerted on particle i by particle j l_{ij}: fraction ($0<l_{ij}<1$) of the line, joining particles i and j that lies within Ω	
(3) $\dfrac{Nk_bT}{V}$ N: number of particles V: volume T: temperature	$\dfrac{1}{3V}\sum_{i=1}^{N-1}\sum_{j>i}\vec{r_{ij}}\cdot\vec{F_{ij}}$ $\vec{r_i}$ and $\vec{r_j}$: positions of particles i and j $\vec{r_{ij}}=\vec{r_i}-\vec{r_j}$ $\vec{F_{ij}}$: force exerted on particle i by particle j	
$\sum_{i=1}^{N} m_i v'_i v'_i \Phi(r-r_i)$ $\Phi(r-r_i)$: Gaussian kernel to spatially smoothen the microscopic data m_i: mass of particle	$-\dfrac{1}{2}\sum_{i=1}^{N}\sum_{j\neq i} r_{ij} F_{ij}\int_{0}^{1} d\lambda\, \Phi(r-r_i-\lambda r_{ij})$ F_{ij}, r_{ij}: magnitude of force and distance between particle i and j	$u(r)=\dfrac{J(r)}{\rho(r)}$ $\rho(r)$: reduced mass density $J(r)$:

(4)	v_i': fluctuating (or thermal) velocity of atom i, $v_i' = v_i - u(r)$ and defined as the difference between the laboratory velocity v_i and streaming velocity u at the location of the function evaluation r	$\Phi(r) = \dfrac{1}{(\sqrt{2\pi w^2})^D} e^{-\frac{|r|^2}{2w^2}}$ D: dimension of the system ω^2:variance: determines the amount of smoothing, while preserving the shape and the area under the curve $\left(\int \Phi(r)dr = 1\right)$	reduced momentum density